Journal of Materials Processing Tech. 305 (2022) 117596

Contents lists available at ScienceDirect

Journal of Materials Processing Tech.

journal homepage: www.elsevier.com/locate/jmatprotec

Effect of chemically accelerated vibratory finishing on the corrosion behavior of Laser Powder Bed Fusion 316L stainless steel

Stephanie Prochaska [a], Owen Hildreth [b,*]

[a] Materials Science Program, Colorado School of Mines, 1500 Illinois St, Golden, CO 80401, USA
[b] Department of Mechanical Engineering, Colorado School of Mines, 1500 Illinois St, Golden, CO 80401, USA

ARTICLE INFO

Associate Editor: Mohsen Seifi

Keywords:
L-PBF 316L
CAVF
Residual stress
Corrosion
Polishing

ABSTRACT

As-built surface morphology and texture of Additively Manufactured (AM) metal parts reduce their mechanical and corrosion properties. One chemically accelerated vibratory finishing (CAVF) technique employs a chemically-based stepwise process to gradually remove surface roughness without the need for significant manual manipulation. While this procedure is effective at producing smooth surfaces, the corrosion response of the resulting surface is unknown. This study evaluates the effect of this surface finishing technique on the corrosion response and mechanisms of 316L stainless steel fabricated using Laser Powder Bed Fusion (L-PBF) AM techniques. The results show that the CAVF process does not obviously change the microstructure but imparts residual compressive stresses on the surface which improve the breakdown potential compared to other specimens evaluated. Further, the process removed surface Cr_3C_2 precipitates formed during heat treatment. CAVF improves surface finish and mechanical properties with an added benefit of enhancing the corrosion response of processed parts.

1. Introduction

Components produced using Additive Manufacturing (AM) Laser Powder Bed Fusion (L-PBF) process are often extremely rough. In addition to esthetic implications, Solberg et al. (2019) showed that part surface roughness decreases the part's fatigue life compared to conventional metals, particularly under low load-high cycle conditions. Kantzos et al. (2018) further described how each valley on the AM surface increases the amount of localized stress, resulting in a potential crack initiation site. From there, crack propagation can occur under application of cyclic loads. According to Ye et al. (2021), multiple, converging micro cracks can proliferate across surface defects and eventually lead to part failure. In addition to fatigue performance, surface roughness influences the corrosion behavior of AM 316L steels, with Melia et al. (2020) showing that rougher surfaces are known to have detrimental effects on the corrosion response. For example, Melia et al. (2020) found that for as-printed L-PBF 316L, surface roughness was the major contributor to corrosion mechanisms, with rougher surfaces eliciting a higher incidence of corrosion concentration cells, thus inferior corrosion properties.

Dundekova et al. (2015) described multiple studies which show polished conventional 316L having either higher or lower corrosion responses compared to the as-received condition. In a 0.5 M NaCl solution, Leban et al. (2014) found conventional stainless steels ground to various roughness between 0.16 and 0.3 μm had similar corrosion potentials while a polished specimen's (0.2 μm) corrosion potential was worse. Another study by Brytan (2016) found that the corrosion resistance of stainless steel alloys significantly decreases when R_a increases above 0.5 μm. Many methods exist to mechanically smooth printed surfaces to improve fatigue and corrosion properties, according to Peng et al. (2021). A variety of bulk methods can be employed on larger surface areas or can encompass entire parts; these methods include surface mechanical attrition treatment (SMAT) (Sun et al., 2019), sandblasting (Mesicek et al., 2021), self-terminating etching processes (STEP) (Hoffman et al., 2020), shot peening (Walczak and Szala, 2021), and chemically accelerated vibratory finishing (CAVF) (Witkin et al., 2019).

SMAT describes peening and blasting techniques which result in nanocrystallization of the resulting surfaces and, in addition to refining surface region grain structure and enhancing fatigue strength, was shown by Sun et al. (2019) to reduce R_a by 96%. Through other surface deformation processes, Mesicek et al. (2021) showed that sandblasting

* Correspondence to: Colorado School of Mines, Department of Mechanical Engineering, Golden, CO 80401, USA.
E-mail address: ohildreth@mines.edu (O. Hildreth).

https://doi.org/10.1016/j.jmatprotec.2022.117596
Received 27 December 2021; Received in revised form 17 February 2022; Accepted 6 April 2022
Available online 8 April 2022

316L parts with aluminum oxide and steel for 2 min reduced R_a by 55%. Further, tumbling parts with plastic and porcelain media resulted in a 68% decrease in R_a, though the process took 120 min. In addition to mechanical surface smoothing, chemical-based processes exist. In one process on AlSi10Mg evaluated by Scherillo (2019), peaks are preferentially attacked during chemical machining due to the formation of insoluble salts which settle into and protect the valley regions. Additionally, Hoffman et al. (2020) showed that a self-terminating etching process involving the sensitization and subsequent electrochemical etching of the top 100–200 μm of a surface has been shown to reduce the surface roughness of 316L stainless steel parts. For AM 17-4PH stainless steel, Walczak and Szala (2021) found that shot peening with ceramic beads improved the corrosion resistance through surface roughness reduction and grain refinement. After a novel CAVF process described by Witkin et al. (2019), the fatigue life of a Ti-6Al-4V part improved by 70 MPa when R_a surface roughness was reduced by approximately 93%. For L-PBF AlSi10Mg, Atzeni et al. (2020) found that the CAVF process reduced part surface roughness to a tenth of the starting roughness, but sharp corners were rounded and part geometry was not fully maintained. Their work also provides a detailed cost-breakdown of the process, ultimately concluding that CAVF does not significantly add to the total cost of printing and post-processing each part. Winklemann et al. (2002) showed that this same process also improved the fatigue life of carburized steel.

While these post-processing techniques focus on improving the mechanical properties, considerations should be made for other important part characteristics that are impacted by surface modification—namely, corrosion properties. The influence of chemical surface modification techniques on the corrosion mechanisms of printed 316L is unstudied yet is an important consideration before these parts are used in real-world, corrosive environments. The CAVF process modifies several material properties that may impact corrosion response. In addition to its primary use for improving part surface roughness, CAVF may also alter microstructure and impart residual stresses, although no previous work exists evaluating these changes for L-PBF 316L and their subsequent effect on corrosion behavior. As previously discussed for similar processes such as shot-peening, grain refinement eliciting an improved corrosion response may be possible. However, changes to grain morphology may be limited for CAVF specimens since the media is primarily used to remove the softened metal and not to mechanically deform the surface. The current work aids in filling some of these knowledge gaps by evaluating L-PBF 316L after having undergone a CAVF process and comparing those results to surfaces prepared through traditional grinding and polishing methods.

This manuscript provides an electrochemical evaluation of 316L stainless steel parts printed with the manufacturer's standard/recommended parameters as well as evaluates the effect of CAVF on the corrosion response of L-PBF 316L. The patented CAVF process called Isotropic Superfinishing (ISF®) was similar to that utilized by Witkin et al. (2019) for improving the fatigue life of Ti-6Al-4V and involves formation of a conversion coating on the base metal through a reaction with proprietary chemistries. The soft conversion coating is mechanically removed from the part, along with surface protrusions, when tumbled with non-abrasive media. The final step is application of an alkaline detergent to clean the surface. The CAVF process utilized in this work has been performed on a variety of metals and alloys, but each alloy requires a unique chemistry formulation. Further, the process is tailored based on the alloy's mechanical or structural response. For example, hardening a material through a heat treatment will reduce the material removal rate, thus potentially requiring an increase in processing time to achieve the desired surface condition. Currently, any part sized to fit inside of the vibrating apparatus can be processed. However, part geometry is the major limitation; internal channels or other tight spaces which are inaccessible to, or which may become plugged by, the tumbling media cannot be treated. As previously described, CAVF does not fully maintain part geometry and tolerances.

2. Materials and methods

2.1. Solids characterization

Printed 316L stainless steel disks (15 mm diameter, 4 mm thick) were used for microstructural characterization and electrochemistry. The samples were printed parallel to the build platform using an EOS M290 Direct Metal Laser Sintering (DMLS) system. Printing parameters were as follows: 214.2 W laser power, 928.1 mm/s scan speed, 100 μm hatch spacing, and 40 μm layer thickness. Cold rolled 316L stainless steel control samples were 4-mm thick disks cut from a sheet using water jet (Big Blue Saw). Table 1 gives the chemical compositions for the L-PBF and control specimens obtained through Auger Electron Spectroscopy. All chemical compositions meet the specification for 316L stainless steels as described by Davis and ASM International (1998).

2.2. Sample preparation

Samples were evaluated in their as-built condition, after heat treatment, and after REM Surface Engineering's (Brenham, Texas) Isotropic Superfinishing (ISF®) process. As a control, cold rolled disks also underwent the CAVF process. The low-temperature ISF® process works as follows: a proprietary processing compound applied to the surface reacts to form a soft chemical conversion coating which is mechanically removed, along with protrusions from the base metal. The conversion coating then reforms on the newly exposed steel and the process repeats until the desired surface finish is achieved. An alkaline cleaning compound terminates the process. All samples were processed at the same time and under the same conditions and the depth of material removed from all surfaces was 400 μm.

To compare the corrosion behavior of as-built disks to heat treated disks, a subset of disks were heat treated under an argon gas environment in a Thermo Scientific Lindberg Blue M tube furnace for one hour and ten minutes at 1060 °C. The ramp rate was 10 °C per minute and specimens underwent quenching in an ice water bath immediately following removal from the furnace. Quenching did not occur under inert gas atmosphere. This heat treatment follows ASTM F3184 (ASTM International, 2016). Heat treated disks were evaluated in the as-printed condition as well as after having undergone the CAVF process.

2.3. Microstructural characterization and electrochemistry

Metallographic specimens were cross-sectioned using a Leco MSX205 sectioning machine and cold mounted in epoxy (EpoFix, Struers). 180, 320, 400, and 600 grit silicon carbide paper (LECO) sequentially ground specimens and they were polished to a one-micron finish using 9 μm, 6 μm, 3 μm, and 1 μm diamond LECO suspensions. All grinding and polishing supplies were used as received. Grain boundaries and phases were revealed through submersing polished metallographic specimens in a solution of 30 mL nitric acid, 60 mL glycerol, and 90 mL hydrochloric acid for 80 s. Stain etched microstructures were imaged with a Zeiss Axio Vert.A1 inverted microscope at magnifications of 3.15 ×, 6.3 ×, 12.6 ×, 31.5 ×, and 63 ×.

To assess phases and crystallographic orientations, X-Ray Diffraction (XRD) using a Bruker AXS D2 Phaser diffractometer from 27° to 130° two theta with a Co Kα source. Surface roughness was quantified using a Bruker DektakXT contact profilometer. Each sample was scanned six times with a 5600 μm-long sampling length (lateral resolution of 0.062 μm) with a 2 μm diameter stylus and 3 mg stylus load. A Gaussian regression filtered data through a short cutoff (λ_s) at 2.5 μm and a long cutoff (λ_c) at 0.8 mm in accordance with the International Organization for Standardization (2015). XRD and profilometry were performed on the up-skin faces of the disks.

A Princeton Applied Research Parstat MC potentiostat performed all electrochemical evaluations. A potassium chloride (KCl) salt bridge ionically connected the silver/silver chloride (4 M Ag/AgCl) reference

Table 1
Chemical composition of printed 316L disks and cold rolled control in wt% (balance Fe).

Material	C	Cr	Mn	Mo	Ni	P	S	Si
Cold rolled 316L	0.021	16.84	1.32	2.08	10.17	0.031	0.007	0.31
L-PBF 316L	0.020	17.65	0.67	2.40	13.15	0.011	0.010	0.62

electrode, and a 6.35-mm diameter graphite rod was the counter electrode. The working electrode was a custom sample holder that exposed 12.5 mm^2 of the disks' up-skin faces to the electrolyte. For all experiments, a 0.6 M sodium chloride (NaCl, 3.5 wt%, Fischer) in deionized water (18 MΩ, Thermo Scientific Smart2Pure 3 UV/UF) electrolyte was prepared. Potentials were reported relative to a standard hydrogen electrode (SHE) by shifting the recorded data by + 0.197 mV. Specimens underwent the following electrochemical tests: Open Circuit Potential (OCP) for 48 h to stabilize the system followed by Cyclic Potentiodynamic Polarization (CPP) from an initial potential of − 1.0 V (vs. OCP) to a vertex potential of + 1 V (vs. OCP) and a scan rate of 10 mV/s. CPP plots provide important insight into the passivation behavior of a metal, including the corrosion potential (E_{corr}), the passivation potential (E_{pp}), the passive film breakdown potential (E_{bd}), and the passive current density (i_{pass}).

To determine the effect, if any, of the surface terminations on the corrosion behavior, the top surface layers of the CAVF and heat treated CAVF specimens were ground with 600 grit silicon carbide paper followed by polishing to a one-micron finish as stated above. Approximately 50 μm of material was removed Electrochemical experiments were repeated on the resurfaced CAVF specimens. For comparison, the surfaces of as-built, heat treated, and cold rolled disks not processed through CAVF were polished and underwent the same electrochemical evaluations.

3. Results and discussion

The corrosion response of any metal depends on multiple properties such as surface features, microstructure, crystallographic orientation, and chemical composition. Surface features can easily dominate and reduce the corrosion response by acting as corrosion concentration cells, as described previously by Melia et al. (2020). The microstructure is important because different phases have different corrosion response. For example, during annealing processes, stainless steels can form detrimental phases such as ferrite which depletes chromium from the matrix and reduces corrosion resistance as found by Chen et al. (2018). The corrosion response of a metal also varies with crystallographic grain orientation. Shahryari et al. (2009) and Krishnan et al. (2013) have shown how pitting resistance is greatly improved for grains oriented in their most densely packed arrangements, with the packing density, thus corrosion rate following the order of {111} < {101} < {001} for face centered cubic austenitic stainless steels.

To understand how the CAVF process impacts corrosion response, we must first determine if there are any microstructural differences before and after CAVF along with any changes to corrosion response. To do this, we will remove the surface features of all specimens through grinding and polishing so that microstructure effects are the only properties measured during electrochemical testing. Once we quantify the influence of microstructure, we will then compare the corrosion response of the as-printed surface to the CAVF processed surface to show how surface features impact corrosion properties.

3.1. Microstructure effects

shows the micrographs of the cold rolled (CR) and CR CAVF specimens. Both micrographs show similarly sized, equiaxed grains. Twinning, a characteristic feature of cold rolled 316L stainless steel microstructures (ASM International and Handbook Committee, 2004), is noted in each specimen's micrograph. The CAVF process resulted in the formation strain induced martensite (α') in the cold rolled specimen, the presence of which is supported by the XRD results showing the characteristic α' peaks in only the CR CAVF diffraction pattern, shown in. Strain induced martensite is known to form in CR austenitic steels and has been previously noted to form by Xiong et al. (2018) and Xu et al. (2018), Santa-aho et al. (2021) documented its formation after shot peening the surface of a CR 316L plate. The same work found that shot peening additively manufactured 316L did not result in formation of α'. Liu et al. (2017) showed how passive film integrity of 316L stainless steels has been shown to degrade with increasing amounts of α' due to microscopic galvanic corrosion between austenite and martensite. Both of those results are consistent to the findings of this work.

As expected, the near-surface microstructures of the L-PBF disks having undergone the low-temperature CAVF process are indistinguishable from as-printed (AB) disks that did not undergo any processing. The near-surface micrographs of AB and CAVF specimens show distinct, finger-like melt pools of equal widths. As typical for as-printed L-PBF 316L microstructures, columnar and cellular grains are seen at and across melt pool boundaries. Cross sectional micrographs further support the lack of bulk microstructural change between the AB and CAVF specimens (Fig. 1). Closer inspection of the surface interfaces reveals a relatively smooth CAVF surface compared to the as-printed disk. Additionally, truncated melt pools at the very top of the CAVF micrograph indicate significant material removal from the surface. Unlike what has been observed after shot-peening, there is no notable grain refinement in the CAVF micrographs. These findings are extended to the heat-treated specimens which show complete microstructure recrystallization and formation of both coarse and fine grains for both as-printed and CAVF specimens. According to Krakhmalev et al. (2018), the annealing temperature was high enough to completely dissolve the columnar and cellular structures. Compared to the cold rolled specimens, grains are generally not equiaxed but elongated in the y-direction (transverse to the specimen surface) and are generally coarser; twinning is present throughout.

The XRD diffraction pattern for the heat treated AB specimen indicates the precipitation of small amounts of chromium carbide (Cr_3C_2). Singh (2016) showed Cr_3C_2 precipitates in the grain boundaries of austenitic stainless steels heated above 1037 °C and cooled too slowly. Boonruang and Sanumang (2021) found nanograin carbide precipitation to occur in a layer between the bulk 316L steel and the outermost passive film. Additionally, the Cr_3C_2 signal was not observed in XRD diffraction patterns for the polished heat treated AB specimen, suggesting the carbides were surface anomalies. Surface and near-surface precipitates may have formed on all heat treated disks but were removed during the CAVF process and through polishing. This is further supported by the lack of Cr_3C_2 in the heat treated CAVF XRD diffraction pattern.

The XRD diffraction patterns for all other specimens evaluated show peaks characteristic of austenite. Peak intensities between the as-printed and CAVF processed specimens do differ, however, with the AB specimen having the strongest (111)γ signal and the heat treated AB specimen having the strongest (200)γ signal of all specimens evaluated. Conversely, both CAVF and heat treated CAVF specimen diffraction patterns showed much smaller (111)γ and (222)γ intensities. Peak intensities increase or decrease with relative number of crystallographic grains oriented along certain planes. From these results, we would expect the AB specimen to have an improved corrosion response since it is more difficult for corrosive species to penetrate the densely packed structures. Conversely, the heat treated AB specimen results are

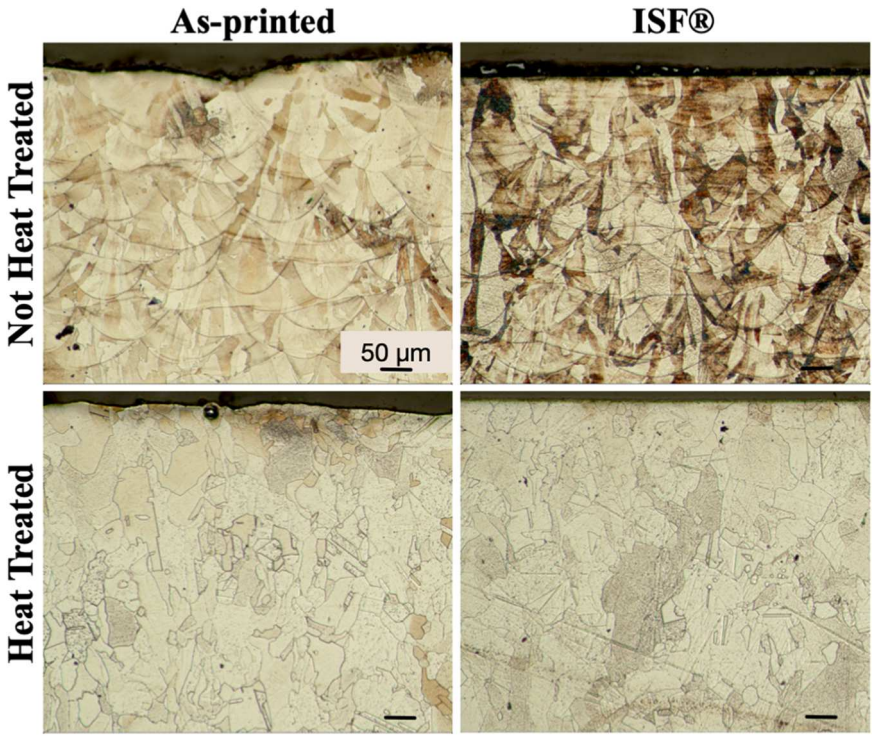

Fig. 1. 12.6 × cross sectional micrographs of as-built and CAVF specimens before and after heat treatment. No major microstructural differences are observed between AB and CAVF conditions, but XRD diffraction patterns indicate precipitation of Cr_3C_2 in the heat treated AB specimen. The heat treatment also fully recrystallized the microstructures and dissolved the columnar and cellular grain structures.

expected to show a decreased corrosion response as the small Cl^- ions can more readily pass through the (200) crystallographic planes. The following section discussing the corrosion response of the specimens verifies this assumption.

To differentiate the dominant influence of surface features and to assess the effect of microstructure on the corrosion response of the AB and CAVF specimens, specimen surfaces were ground and polished before undergoing electrochemical testing. The resulting CPP curves from these polished specimens are in Fig. 2. The CPP results include a polished cold rolled disk for comparison. Table 2 gives the corrosion parameters extracted from the CPP curves in Fig. 2.

Excluding the heat treated AB specimen, all L-PBF polished specimens had E_{corr} between − 0.213 V_{SHE} and − 0.262 V_{SHE}. The cold rolled specimen's E_{corr} was similarly − 0.271 V_{SHE}. Further, the non-heat treated AB and CAVF specimens had very similar E_{pp} and i_{pass} suggesting that the microstructure similarities produced similar corrosion responses. However, both CAVF disks' E_{bd} were significantly higher than those of the AB specimens. In fact, the CAVF specimen didn't have a measurable E_{bd} due to having a positive hysteresis curve (Fig. 3, showing the forward and reverse scan of the CPP) which indicates pitting did not occur over the potential range. One explanation described by Peyre et al. (2000) for the improved pitting resistance of the CAVF specimens is that

Table 2
CPP curve values extracted from Fig. 1; scan rate was 10 mV/s.

Specimen	E_{corr}	E_{pp}	i_{pass} (× 10^{-6})	E_{bd}
Polished CR	-0.271	-0.162	4.13	0.589
Polished AB	-0.253	-0.073	2.25	0.447
Polished HT AB	-0.630	-0.471	30.7	0.329
Polished CAVF	-0.213	-0.092	2.42	–
Polished HT CAVF	-0.262	-0.102	4.88	0.697

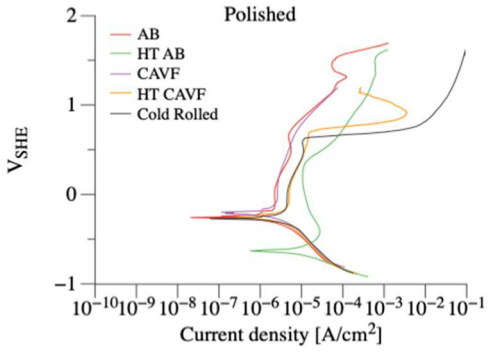

Fig. 2. CPP curves for the polished AB, CAVF, and cold rolled 316L stainless steel specimens. The E_{corr} for the AB and both CAVF specimens converged to a similar value while the heat treated AB had the most negative E_{corr} of all evaluated disks. The scan rate was 10 mV/s.

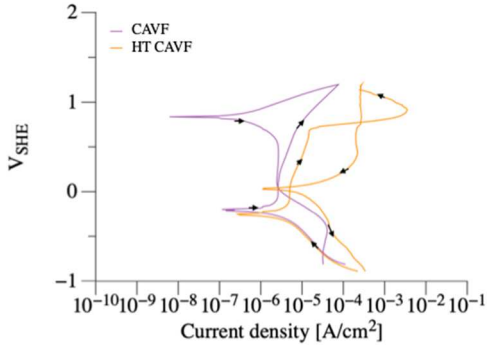

Fig. 3. CPP curves for the polished CAVF and heat treated CAVF 316L stainless steel specimens. The CPP curve for the CAVF specimen shows a positive hysteresis loop indicating pitting did not occur over the potential range. The CPP curve for the heat treated CAVF specimen had a negative (though relatively small) hysteresis loop suggesting pitting occurred. The scan rate was 10 mV/s.

the vibratory process introduced residual compressive stress to the surface which reduce pit formation. Multiple previous studies on conventional 316L stainless steel have obtained similar results through a variety of work hardening processes including shot peening (Azar et al., 2010) and laser shock peening (Ebrahimi et al., 2017). According to Liu and Frankel (2006), residual compressive stresses decrease the number of active sites on the surface, thus impeding initiation and propagation of corrosion. Their work also found that compressive stresses improve the longevity and strength of the passive film by making the film more difficult to rupture.

Since the E_{bd} of the AB and CAVF disks are different after resurfacing, the depth of the induced compressive stresses exceeded the depth of material removed during the resurfacing of the CAVF specimens, thus preserving the pitting protection mechanism. Further, the compressive layer of the HT CAVF disk likely does not penetrate as far into the bulk as that of the CAVF disk due to the heat treatment hardening the material. This therefore impedes the E_{bd} improvement for the HT CAVF disk.

The polished heat treated AB disk had appreciably more negative E_{corr}, E_{pp}, and E_{bd} to the other specimens evaluated. Additionally, the i_{pass} was an order of magnitude larger than the i_{pass} of other specimens, indicating formation of a much less dense passive layer. In the absence of influence from surface features, the poorer corrosion properties are due to the incidence of crystallographic grains oriented in the least-closely packed (200)γ.

3.2. Surface effects

After verification that the CAVF process doesn't have a substantial impact on the corrosion potential from a microstructure perspective other than the increase in E_{bd}, the effect of the inherent surface morphology on the corrosion properties was evaluated. Surface roughness was measured on the heat treated and non-heat treated AB and CAVF disks in their as-printed and post-processed conditions; there was no subsequent surface polishing. Specimens underwent electrochemical testing to determine how surface roughness and the surface terminations resulting from the CAVF process influence corrosion.

Surface roughness can be measured through contact profilometry and described by the roughness profile, R_a. R_a is the roughness profile representing the arithmetical mean deviation of the evaluated profile as described by Whitehouse (2004) in Eq. (1) and is derived from the primary profile by filtering out surface waviness and longer wavelengths (International Organization for Standardization, 2015).

$$R_a = \frac{1}{l_r}\int_0^{l_r} |z(x)|\ dx \quad (1)$$

Where l_r is the sampling length and z(x) is the profile ordinates of the roughness profile (Mitutoyo, 2016).

The cold rolled disk's average R_a surface roughness was 1.88 ± 0.43 μm as shown in Fig. 4. The average surface roughness value for the cold rolled disk processed through CAVF, not shown in the figure, was 0.040 ± 0.01 μm. As expected, the AB and heat treated AB specimens have the highest average R_a roughness values of all specimens evaluated, 4.55 ± 0.81 μm and 3.77 ± 1.40 μm, respectively. The heat treatment had no major effect on the surface roughness of the AB disks. The standard deviation for the AB disk was less than that of the heat treated AB disk, suggesting insignificant differences in surface roughness. Comparatively, the CAVF specimens had average R_a values of 0.043 ± 0.01 μm for the as-printed CAVF disk and 0.063 ± 0.03 μm for heat treated CAVF. Since material removal rates are lower for harder materials, the CAVF process removed less material from the heat treated disks compared to the non-heat treated disks. Due to the stepwise nature of the CAVF process, additional processing steps can further refine the surface texture. The average R_a surface roughnesses for the polished specimens were 0.015 ± 0.01 μm, as depicted by the solid red line.

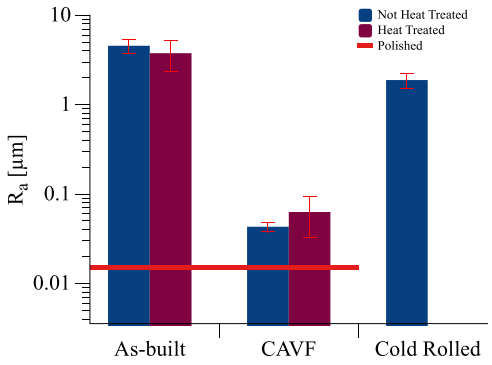

Fig. 4. R_a surface roughness values for as-built and heat treated as-printed and CAVF disks. Manual polishing resulted in the lowest roughnesses of all surfaces measured.

Supplementary Fig. 4 a–c show the R_z, R_v, and R_{sk} parameters, respectively, for the as-built and CAVF specimens. R_z, the maximum roughness along the sampling length, follows similar trends as R_a roughness for the as-built specimens. The R_z roughness for both of the CAVF specimens was the same. A component of R_z, R_v denotes the lowest measured valley across the sampling length. Both non-heat treated as-built and CAVF specimens had deeper valleys than the heat-treated versions, another indication of material hardening resulting in a lower material removal rate. Finally, skewness, R_{sk}, for the CAVF specimens is more negative than that of the as-built specimens indicating the CAVF surfaces are mainly valleys while the as-built surfaces are comprised mostly of peaks and other protrusions. This result is not unexpected as the CAVF process preferentially smooths surface peaks.

The CPP curves for unpolished (non-resurfaced) AB and CAVF specimens are in Fig. 5. Corrosion parameters extracted from the curves are in Table 3. E_{corr} results are similar for the CR and CAVF cold rolled disks, with the un-post processed disk having a value approximately 0.060 V_{SHE} more positive despite having a much rougher surface. Similarly, E_{pp} becomes more negative with post-processing, indicating the disruption of the surface passivation layer. This finding is supported by the cold rolled disk having a smaller i_{pass} (indicating a denser passive layer) than the CAVF cold rolled specimen. The strain induced martensite did not noticeably impact the corrosion response of the CAVF cold rolled specimen. The CR CAVF and polished CR specimen had nearly identical corrosion parameters which were slightly worse than the cold rolled specimen.

Analogously to the unprocessed cold rolled disk, a dense passive film on the AB disk elicited the most positive E_{corr} and E_{pp} of all printed specimens evaluated, − 0.151 V_{SHE} and − 0.041 V_{SHE}, respectively. These results signify that despite having rough surfaces, the native

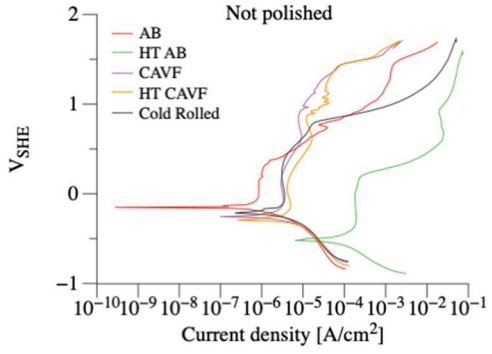

Fig. 5. CPP curves for the unpolished AB and CAVF 316L stainless steel. The AB specimen had the most positive E_{corr} and heat treated AB had the most negative E_{corr} of all evaluated disks. CAVF processing resulted in heat treated and non-heat treated disks having similar E_{corr}. The scan rate was 10 mV/s.

Table 3
CPP curve values extracted from Fig. 5; scan rate was 10 mV/s.

Specimen	E_{corr}	E_{pp}	i_{pass} ($\times 10^{-6}$)	E_{bd}
Cold Rolled	-0.215	-0.065	3.57	0.784
CR CAVF	-0.272	-0.132	4.07	0.698
AB	-0.151	-0.041	0.87	0.269
HT AB	-0.537	-0.357	35.8	0.053
CAVF	-0.254	-0.114	3.32	1.117
HT CAVF	-0.291	-0.161	4.95	0.878

passivation layers on specimens that are not post-processed readily provide comparatively good corrosion protection. However, it is important to note that the E_{bd} of the AB disks were significantly lower than the E_{bd} of all other specimens implying a much smaller range of potentials with improved pitting resistance ($E_{bd} - E_{corr}$) before the breakdown of the passive film. This result is supported by the greater number of pit initiation sites inherent of the rougher surface and the observation that E_{bd} for both AB disks increased upon reduction of those sites through resurfacing.

While the CAVF process doesn't appear to greatly affect E_{corr}, E_{pp}, or i_{pass}, it again significantly improved the E_{bd} of as-printed CAVF and heat treated CAVF, which consequently had the largest $E_{bd} - E_{corr}$ of all evaluated specimens of 1.117 V_{SHE} and 0.878 V_{SHE}, respectively. This finding is congruent to the polished CAVF and CR CAVF specimens' improvements in E_{bd} and high pitting resistance and is due to the compressive stresses incurred through the CAVF process. The HT CAVF specimen had a higher E_{bd} than its resurfaced counterpart therefore indicating that the compressive stress layer and corresponding pitting protection was notably diminished through subsequent grinding and polishing. Because the unpolished CAVF specimens had a slightly rougher surface than when polished, E_{corr}, E_{pp}, and i_{pass} indicated worse corrosion performance though to a largely insignificant extent. Surface roughness increased the average potential for CAVF specimen E_{corr} and E_{pp} by 0.038 V.

As with the polished specimens, the heat treatment appreciably worsened the corrosion properties of the heat treated AB specimen, resulting in an E_{corr} of − 0.537 V_{SHE} and i_{pass} of 35.8 $\times 10^{-6}$ A/cm^2—the least dense passive film of all evaluated specimens. Surface roughness improved E_{corr} by 0.1 V between the polished and unpolished specimens, but E_{bd} decreased by 0.276 V due to the increase in pit initiation sites. Despite XRD diffraction patterns indicating precipitation of Cr_3C_2 which depletes chromium in the grain boundaries and leads to sensitization of the steel and decreased corrosion resistance, the most likely explanation for the poor corrosion response of the heat treated AB specimens is again the prevalence of (200)γ peaks. Crystallographic grain orientation may also explain the superior E_{pp} and i_{pass} of the (111)γ-rich AB specimens. The non-carbide containing heat treated CAVF specimen had E_{corr} values in the range typical for the non-heat treated CAVF specimens. It is possible that the CAVF process fully removed any formed carbide layer from the heat treated CAVF specimen, whereas re-grinding and polishing alone (as for the polished heat treated AB specimen) did not.

Ultimately, there is minor variation in surface roughness between all post-processed specimens. Congruent to previously described findings by Leban et al. (2014) and Dundekova et al. (2015), once R_a roughness decreased below approximately 0.1 μm, E_{corr} converged to values in the range of − 0.291 V_{SHE} to − 0.213 V_{SHE}, suggesting surface roughness as the dominating mechanism controlling corrosion potential with smaller R_a achieving better corrosion properties. E_{pp} also decreases with increasing surface roughness. This finding is not extended to the AB and cold rolled specimen which had rougher surfaces but higher E_{pp} to form dense passivation layers which improved E_{corr}. Additionally, E_{corr} of the heat treated AB specimens is controlled by crystallographic orientation of grains in (200)γ.

While CAVF resulted in limited E_{corr} improvement, the process greatly enhances E_{bd} for both heat treated and non-heat treated specimens. The polished CAVF specimen's corrosion properties nearly matched those of the cold rolled specimen, however the CAVF disk never pitted during electrochemical testing. Generally, for L-PBF specimens, surface smoothing enhances E_{bd}.

4. Conclusions

Just as it is important to refine as-built additively manufactured surfaces for fatigue performance, it is also critical to consider the potential change in corrosion properties that may result from these processes. This work evaluated the corrosion behavior of as-built and heat-treated L-PBF and cold rolled 316L stainless steel specimens having undergone Isotropic Superfinishing, a novel, chemically activated vibratory finishing process. Those results were compared with corrosion results from as-built and heat-treated L-PBF 316L specimens in the as-printed and polished conditions. The most important finding of this work is that the CAVF process greatly improved the corrosion behavior of heat-treated L-PBF 316L stainless steel and future work should focus on determining the mechanisms of that improvement. Utilizing the CAVF process does not have detrimental impacts to the resulting electrochemical properties of L-PBF 316L stainless steel and, in many cases, improves the corrosion resistance compared to as-built and conventionally polished specimens.

Additional major findings of this work are as follows:

- The CAVF process formed strain induced martensite in the cold rolled specimen, but there was no resulting impact on corrosion response.
- CAVF had no effect on E_{corr}, E_{pp}, or i_{pass}, but E_{bd} improved significantly, up to 1.1 V, compared to all other specimens due to residual compressive stresses impeding pit initiation. Higher E_{bd} was retained post-resurfacing. Longer-term exposure to corrosive environments and subsequent re-evaluation of electrochemical properties should be conducted to determine the durability and/or longevity of the CAVF surface.
- Heat treatment was highly detrimental to the corrosion resistance of the as-built specimen; chromium carbides precipitated, and the steel was sensitized. The CAVF process either removed the carbides or inhibited their impact on corrosion behavior.
- CAVF processing resulted in surfaces with R_a values less than 0.1 μm. Surface roughness dominated the corrosion potential for all post-processed specimens (excluding heat treated AB specimens), with all E_{corr} converging to between − 0.291 V_{SHE} and − 0.213 V_{SHE} when R_a was small.

CRediT authorship contribution statement

Stephanie Prochaska: Conceptualization, Methodology, Investigation, Formal analysis, Writing – original draft. **Owen Hildreth:** Funding acquisition, Resources, Writing – review & editing, Supervision.

Declaration of Competing Interest

The authors declare the following financial interests/personal relationships which may be considered as potential competing interests: Owen J. Hildreth reports financial support was provided by National Science Foundation.

Acknowledgements

This material is based upon work supported by the National Science Foundation under Grant no. CAREER 1944516. The authors would also like to thank and acknowledge REM Surface Engineering for performing the ISF® process on the specimens used in this work.

Appendix A. Supporting information

Supplementary data associated with this article can be found in the online version at doi:10.1016/j.jmatprotec.2022.117596.

References

ASM International, Handbook Committee, 2004. Metallography and Microstructures of Ferrous Alloys. ASM International, Materials Park, OH.

Ye, C., Zhang, C., Zhao, J., Dong, Y., et al., 2021. Effects of post-processing on the surface finish, porosity, residual stresses, and fatigue performance of additive manufactured metals: A review. Journal of Materials Engineering and Performance. https://doi.org/10.1007/s11665-021-06021-7.

ASTM International, 2016. ASTM F3184-16, Standard Specification for Additive Manufacturing Stainless Steel Alloy (UNS S31603) with Powder Bed Fusion. West Conshohocken, PA.

Atzeni, E., Balestrucci, A., Catalano, A.R., Iuliano, L., Priarone, P.C., Salmi, A., Settineri, L., 2020. Performance assessment of a vibro-finishing technology for additively manufactured components. Procedia CIRP 88, 427–432. https://doi.org/10.1016/j.procir.2020.05.074.

Azar, V., Hashemi, B., Rezaee Yazdi, M., 2010. The effect of shot peening on fatigue and corrosion behavior of 316L stainless steel in Ringer's solution. Surf. Coat. Technol. 204, 3546–3551. https://doi.org/10.1016/j.surfcoat.2010.04.015.

Boonruang, C., Sanumang, W., 2021. Effect of nano-grain carbide formation on electrochemical behavior of 316L stainless steel. Sci. Rep. 11, 12602. https://doi.org/10.1038/s41598-021-91958-x.

Brytan, Z., 2016. The passivation treatment of stainless steel surface studied by electrochemical impedance spectroscopy. Presented at the The 2016 World Congress on Advances in Civil, Environmental, and Materials Research, Jeju Island, Korea.

Chen, X., Li, J., Cheng, X., Wang, H., Huang, Z., 2018. Effect of heat treatment on microstructure, mechanical and corrosion properties of austenitic stainless steel 316L using arc additive manufacturing. Mater. Sci. Eng. A 715, 307–314. https://doi.org/10.1016/j.msea.2017.10.002.

Davis, J.R., International, A.S.M. (Eds.), 1998. Metals Handbook, Desk ed., 2nd ed. ASM International, Materials Park, Oh.

Dundekova, Sylvia, Zatkalikova, Viera, Fintova, Stanislava, Hadzima, Branislav, Skorik, Viktor, 2015. Influence of the surface finishing on the corrosion behaviour of AISI 316L stainless steel. Mater. Eng. - Mater. Inž. 22, 48–53.

Ebrahimi, M., Amini, S., Mahdavi, S.M., 2017. The investigation of laser shock peening effects on corrosion and hardness properties of ANSI 316L stainless steel. Int. J. Adv. Manuf. Technol. 88, 1557–1565. https://doi.org/10.1007/s00170-016-8873-0.

Hoffman, R., Hinnebusch, S., Raikar, S., To, A.C., Hildreth, O.J., 2020. Support thickness, pitch, and applied bias effects on the carbide formation, surface roughness, and material removal of additively manufactured 316 L stainless steel. JOM. https://doi.org/10.1007/s11837-020-04422-y.

International Organization for Standardization, 2015. ISO 4287:1997 Geometrical Product Specifications (GPS) – Surface Texture: Profile Method – Terms, Definitions and Surface Texture Parameters. International Organization for Standardization.

Kantzos, C., Cunningham, R., Tari, V., Rollett, A., et al., 2018. Characterization of metal additive manufacturing surfaces using synchrotron x-ray CT and micromechanical modeling. Computational Mechanics. https://doi.org/10.1007/s00466-017-1531-z.

Krakhmalev, P., Fredriksson, G., Svensson, K., Yadroitsev, I., Yadroitsava, I., Thuvander, M., Peng, R., 2018. Microstructure, solidification texture, and thermal stability of 316 L stainless steel manufactured by laser powder bed fusion. Metals 8, 643. https://doi.org/10.3390/met8080643.

Krishnan, S., et al., 2013. Effect of crystallographic orientation on the pitting corrosion resistance of laser surface melted AISI 304L Austenitic stainless steel. International Journal of Mechanical and Mechatronics Engineering 7 (4), 650–653.

Leban, M.B., Mikyška, Č., Kosec, T., Markoli, B., Kovač, J., 2014. The effect of surface roughness on the corrosion properties of type AISI 304 stainless steel in diluted NaCl and urban rain solution. J. Mater. Eng. Perform. 23, 1695–1702. https://doi.org/10.1007/s11665-014-0940-9.

Liu, X., Frankel, G., 2006. Effects of compressive stress on localized corrosion in AA2024-T3. Corrosion Science. https://doi.org/10.1016/j.corsci.2005.12.003.

Liu, E., Zhang, Y., Zhu, L., Zeng, Z., Gao, R., 2017. Effect of strain-induced martensite on the tribocorrosion of AISI 316L austenitic stainless steel in seawater. RSC Adv. 7, 44923–44932. https://doi.org/10.1039/C7RA07318F.

Melia, M.A., Duran, J.G., Koepke, J.R., Saiz, D.J., Jared, B.H., Schindelholz, E.J., 2020. How build angle and post-processing impact roughness and corrosion of additively manufactured 316L stainless steel. Npj Mater. Degrad. 4, 21. https://doi.org/10.1038/s41529-020-00126-5.

Mesicek, J., Ma, Q.-P., Hajnys, J., Zelinka, J., Pagac, M., Petru, J., Mizera, O., 2021. Abrasive surface finishing on SLM 316L parts fabricated with recycled powder. Appl. Sci. 11, 2869. https://doi.org/10.3390/app11062869.

Mitutoyo Quick Guide to Surface Roughness Measurement (Bulletin No. 2229) 2016.

Peng, X., Kong, L., Fuh, J.Y.H., Wang, H., 2021. A review of post-processing technologies in additive manufacturing. J. Manuf. Mater. Process 5, 38. https://doi.org/10.3390/jmmp5020038.

Peyre, P., Scherpereel, X., Berthe, L., Carboni, C., Fabbro, R., Béranger, G., Lemaitre, C., 2000. Surface modifications induced in 316L steel by laser peening and shot-peening. Influence on pitting corrosion resistance. Mater. Sci. Eng. A280, 294–302.

Santa-aho, S., et al., 2021. Additive manufactured 316L stainless steel samples: Microstructure, Residual Stress and Corrosion Characteristics after Post-Processing. Metals. https://doi.org/10.3390/met11020182.

Scherillo, F., 2019. Chemical surface finishing of AlSi10Mg components made by additive manufacturing. Manuf. Lett. 19, 5–9. https://doi.org/10.1016/j.mfglet.2018.12.002.

Shahryari, A., Szpunar, J., Omanovic, S., et al., 2009. The influence of crystallographic orientation distribution on 316LVM stainless steel pitting behavior. Corrosion Science 51 (3). https://doi.org/10.1016/j.corsci.2008.12.019.

Singh, R., 2016. Stainless steels. In: Applied Welding Engineering. Elsevier, pp. 83–90. https://doi.org/10.1016/B978-0-12-804176-5.00008-6.

Solberg, K., Guan, S., Razavi, S., Welo, T., Chan, K., Berto, F., et al., 2019. Fatigue of additively manufactured 316L stainless steel: The influence of porosity and surface roughness. Fatigue & Fracture of Engineering Materials & Structures 42 (9). https://doi.org/10.1111/ffe.13077.

Sun, Y., Bailey, R., Moroz, A., 2019. Surface finish and properties enhancement of selective laser melted 316L stainless steel by surface mechanical attrition treatment. Surf. Coat. Technol. 378, 124993 https://doi.org/10.1016/j.surfcoat.2019.124993.

Walczak, M., Szala, M., 2021. Effect of shot peening on the surface properties, corrosion and wear performance of 17-4PH steel produced by DMLS additive manufacturing. Arch. Civ. Mech. Eng. 21, 157. https://doi.org/10.1007/s43452-021-00306-3.

Whitehouse, D., 2004. Surfaces and their Measurement, 1st ed. Butterworth-Heinemann, Oxford.

Winklemann, L., Michaud, M., Sroka, G., Swiglo, A.A., 2002. Impact of isotropic superfinishing on contact and bending fatigue of carburized steel. In: Advances in Surface Engineering. Presented at the SAE International, SAE International, Las Vegas, p. 13.

Witkin, D.B., Patel, D.N., Helvajian, H., Steffeney, L., Diaz, A., 2019. Surface treatment of powder-bed fusion additive manufactured metals for improved fatigue life. J. Mater. Eng. Perform. 28, 681–692. https://doi.org/10.1007/s11665-018-3732-9.

Xiong, Y., Yue, Y., He, T., Lu, Y., Ren, F., Cao, W., 2018. Effect of rolling temperature on microstructure evolution and mechanical properties of AISI316LN austenitic stainless steel. Materials 11, 1557. https://doi.org/10.3390/ma11091557.

Xu, D., Wan, X., Yu, J., Xu, G., Li, G., 2018. Effect of cold deformation on microstructures and mechanical properties of austenitic stainless steel. Metals 8, 522. https://doi.org/10.3390/met8070522.